nanomaterials

MDPI

Article

A Facile Pre-Lithiated Strategy towards High-Performance Li_2Se-$LiTiO_2$ Composite Cathode for Li-Se Batteries

Yang Xia [1], Zheng Fang [1], Chengwei Lu [1,*], Zhen Xiao [2], Xinping He [1], Yongping Gan [1], Hui Huang [1], Guoguang Wang [3] and Wenkui Zhang [1,*]

[1] College of Materials Science and Engineering, Zhejiang University of Technology, Hangzhou 310014, China; nanoshine@zjut.edu.cn (Y.X.); 2111925054@zjut.edu.cn (Z.F.); xinpinghe@zjut.edu.cn (X.H.); ganyp@zjut.edu.cn (Y.G.); hhui@zjut.edu.cn (H.H.)
[2] Institute of Optoelectronic Materials and Devices, China Jiliang University, Hangzhou 310018, China; xiaozhen@cjlu.edu.cn
[3] Hengdian Group DMEGC Magnetics Co., Ltd., Dongyang 322118, China; wgg@dmegc.com.cn
* Correspondence: lcw5460@zjut.edu.cn (C.L.); msechem@zjut.edu.cn (W.Z.)

Abstract: Conventional lithium-ion batteries with a limited energy density are unable to assume the responsibility of energy-structure innovation. Lithium-selenium (Li-Se) batteries are considered to be the next generation energy storage devices since Se cathodes have high volumetric energy density. However, the shuttle effect and volume expansion of Se cathodes severely restrict the commercialization of Li-Se batteries. Herein, a facile solid-phase synthesis method is successfully developed to fabricate novel pre-lithiated Li_2Se-$LiTiO_2$ composite cathode materials. Impressively, the rationally designed Li_2Se-$LiTiO_2$ composites demonstrate significantly enhanced electrochemical performance. On the one hand, the overpotential of Li_2Se-$LiTiO_2$ cathode extremely decreases from 2.93 V to 2.15 V. On the other hand, the specific discharge capacity of Li_2Se-$LiTiO_2$ cathode is two times higher than that of Li_2Se. Such enhancement is mainly accounted to the emergence of oxygen vacancies during the conversion of Ti^{4+} into Ti^{3+}, as well as the strong chemisorption of $LiTiO_2$ particles for polyselenides. This facile pre-lithiated strategy underscores the potential importance of embedding Li into Se for boosting electrochemical performance of Se cathode, which is highly expected for high-performance Li-Se batteries to cover a wide range of practical applications.

Keywords: Li-Se batteries; Li_2Se; $LiTiO_2$; pre-lithiation; polyselenides

Citation: Xia, Y.; Fang, Z.; Lu, C.; Xiao, Z.; He, X.; Gan, Y.; Huang, H.; Wang, G.; Zhang, W. A Facile Pre-Lithiated Strategy towards High-Performance Li_2Se-$LiTiO_2$ Composite Cathode for Li-Se Batteries. *Nanomaterials* **2022**, *12*, 815. https://doi.org/10.3390/nano12050815

Academic Editor: Christian M. Julien

Received: 6 February 2022
Accepted: 25 February 2022
Published: 28 February 2022

1. Introduction

In recent years, the conventional lithium-ion batteries cannot meet the current development demand due to the limited energy density [1–9]. In this respect, sulfur cathode offers a high theoretical specific capacity of 1675 mA h g^{-1} when paired with lithium metal anode [10–12]. Ironically, lithium-sulfur batteries are mainly limited by non-conductive feature of sulfur cathode [13–15]. Selenium (Se), as an agnate element of sulfur, has similar charge-discharge reaction and volumetric capacity to sulfur, and the electronic conductivity of Se (1×10^{-3} S m^{-1}) is much higher than sulfur (5×10^{-28} S m^{-1}) [16,17]. Hence, Li-Se batteries are considered as one of the new generations of promising electrochemical energy storage devices [18–21]. However, the development of Li-Se batteries still faces many problems, such as notorious shuttle effect and volume expansion in Li^+ insert/extract processes, which cause the loss of active material and low Coulombic efficiency. Meanwhile, the intermediate products (polyselenides) dissolve in ether-based electrolyte and further migrate to the anode side, which will not only passive the surface of lithium metal anode, but also severely reduce the cyclic performance [22–27].

Up to now, many strategies are adopted to circumvent the abovementioned concerns to facilitate the electrochemical performance of Li-Se batteries. The introduction of TiO_2

as secondary phase for Li-S/Se batteries is demonstrated to be an effective strategy on account of its strong chemisorption of lithium polysulfides/lithium polyselenides [14,28–31]. However, the synthesis of TiO_2/Se composite is cumbersome, and the volume expansion is still unresolvable. It is worth mentioning that the pre-lithiation of Se is a valid strategy to mitigate the volume expansion [32–34]. Unfortunately, the synthesis of fully lithiated Li_2Se often involves complex processes and expensive chemical reagents, which remains huge challenges in great urgency [33–35]. Therefore, the key to break this predicament is the concise and efficient synthesis of fully pre-lithiated Se-based composites.

In this work, as illustrated in Figure 1, we propose a novel Li_2Se-$LiTiO_2$ composite cathode, which is obtained via a two-step solid-phase method. During the synthesis process, LiH synchronously reacts with Se and TiO_2 to in-situ form Li_2Se-$LiTiO_2$ composite and by-product H_2 gas, which needs no subsequent separation. As the fully pre-lithiated cathode, Li_2Se-$LiTiO_2$ composite has many unique features. On the one hand, Li_2Se could easily ameliorate the volume expansion, thereby leading to the superior structure stability and enhanced cycling stability. On the other hand, the introduced $LiTiO_2$ not only could accelerate the reaction kinetics and electrochemical activities of Li_2Se, reducing the reaction overpotential, but also offer the abundant chemical adsorption sites for tapping polyselenides, suppressing the notorious shuttle effect. Therefore, this rationally designed Li_2Se-$LiTiO_2$ composite is a promising Se-based cathode for high-performance Li-Se batteries.

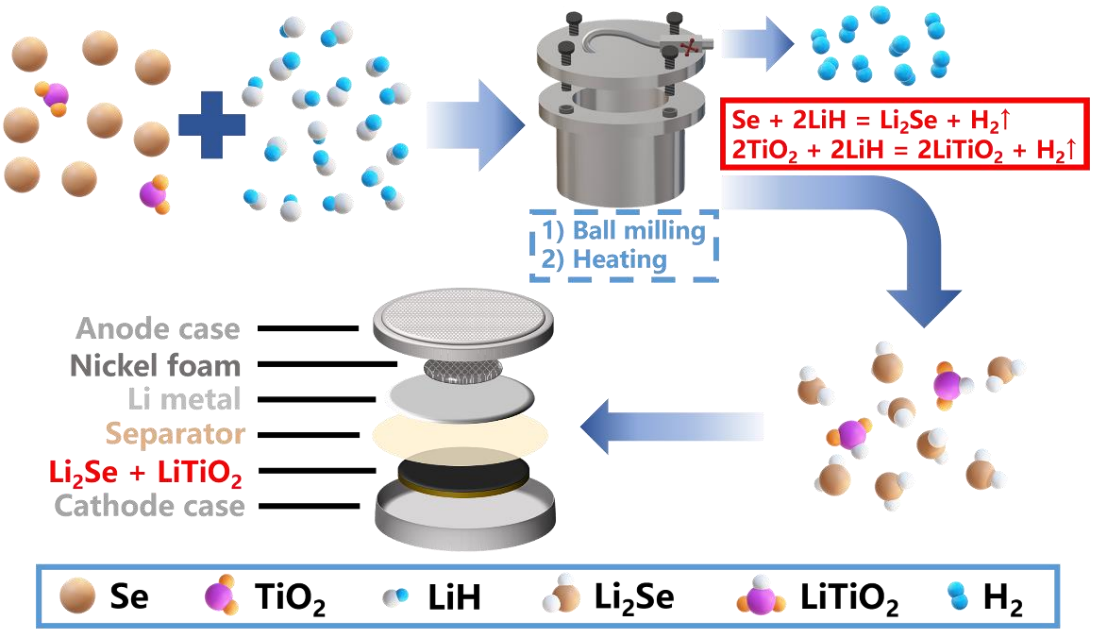

Figure 1. Schematic illustration of the preparation process of Li_2Se-$LiTiO_2$ composites.

2. Experimental Section

2.1. Preparation of Li_2Se-$LiTiO_2$ Composites

Selenium powder (Se, Aladdin Holdings Group Co. Ltd., Shanghai, China, purity 99.99%), anatase phase titanium dioxide (TiO_2, Aladdin Holdings Group Co. Ltd., Shanghai, China, purity 99.8%) and lithium hydride (LiH, Aladdin Holdings Group Co. Ltd., Shanghai, China, purity 97%) were used without further purification. Li_2Se-$LiTiO_2$ samples were synthesized via two-step solid-phase reaction. In detail, Se, TiO_2 and LiH powders were transferred into stainless-steel milling jars with a molar ratio of 4:1:9. The milling jars were milled on a planetary ball mill (QM-1SP2, Nanjing university instrument factory, Nanjing, China) at 500 rpm for 20 h. After that, the precursor was heated in a custom tube reactor at 500 °C for 3 h under vacuum to obtain Li_2Se-$LiTiO_2$ composites.

2.2. Materials Characterization

X-ray diffraction (XRD) patterns were carried out by an X-ray powder diffractometer (X'Pert Pro, Cu Kα radiation, Rigaku Corporation, Tokyo, Japan). All the samples were sealed with Kapton film to avoid air exposure. The morphology and microstructure were observed by scanning electron microscopy (SEM, Nova Nano 450, FEI, Hillsboro, OR, USA) with an energy dispersive spectroscopy (EDS, Oxford X-Max 80, Oxford Instruments, Oxford, UK) detector and transmission electron microscopy (TEM, Tecnai G2 F30, FEI, Hillsboro, OR, USA). X-ray photoelectron spectroscopy (XPS, ESCALAB 250X, Themo, Shanghai, China) measurements were performed on an Axis Ultra DLD system (Kratos) with a monochromatic Al Kα (1486.6 eV) X-ray source. Ultraviolet-visible (UV-vis) adsorption spectra were recorded on SHIMADSU UV-2550 spectrophotometer (SHIMADSU, Chengdu, China) to assess the polyselenide adsorption ability.

2.3. Electrochemical Measurements

Electrochemical properties of Li_2Se-$LiTiO_2$ electrodes were conducted on CR2025-type coin cells by using lithium metal as anode. The uniform slurry was composed of 60 wt.% Li_2Se-$LiTiO_2$ composite as active material, 30 wt.% conductive carbon (Super P, SP) and 10 wt.% ethyl cellulose, which were mixed by toluene as dispersant. The electrolyte was 1.0 mol L^{-1} lithium bis(trifluoromethanesulfonyl)imide (LiTFSI) in a co-solvent of 1,3-dioxolane (DOL)/1,2-dimethoxyethane (DME) (1:1, *v*/*v*) with 2 wt.% lithium nitrate ($LiNO_3$). The electrolyte dosage in each cell was 20 μL mg^{-1} of electrolyte-to-active material ratio. All the cells were assembled in an Ar-filled glove box (H_2O < 0.1 ppm, O_2 < 0.1 ppm). The galvanostatic charge-discharge tests were performed on a battery testing system (Shenzhen Neware Technology Co. Ltd., Shenzhen, China). The cells were firstly charged to 3.8 V at 50 mA g^{-1}, and subsequently the voltage window was adjusted to 1.7–2.6 V. For cyclic voltammogram (CV) analysis, the first forward scan started from open circuit voltage to 3.8 V, and a backward scan ended to 1.7 V. The successive scans were in the voltage range of 1.7–2.6 V at a scan rate of 0.1 mV s^{-1} on CHI650B electrochemical workstation (Chenhua, Shanghai, China). Electrochemical impedance spectra (EIS) were recorded in the frequency range from 0.1 Hz to 1.0 MHz on CHI650B electrochemical workstation.

3. Results and Discussion

In order to reveal the reaction mechanism of Li_2Se-$LiTiO_2$ composite by reacting LiH with Se and TiO_2, Figure 2a,b illustrate the time-pressure curves for the ball-milling and heating processes, respectively. During the initial ball-milling process, the pressure increases dramatically to 3.39 bar within 1 h, suggesting the reaction generates a large amount of gas. Subsequently, the pressure slowly raises to 3.63 bar from 1 h to 10 h. After 10 h, the gas is no longer produced, indicating the ball-milling reaction is completed. Meanwhile, during the heating process, a conspicuous variation in pressure can be detected, in which the pressure is rapidly increased in the temperature ranging from 250 °C to 400 °C. This result implies that LiH reacts with Se and TiO_2 in this temperature range. In order to prove the phase transformation after ball-milling and heating processes, the corresponding XRD patterns of Li_2Se-$LiTiO_2$, Li_2Se and $LiTiO_2$ are depicted in Figure 2c. The diffraction peaks of Li_2Se-$LiTiO_2$ composite shows a superposition of Li_2Se (PDF#23-0072) and $LiTiO_2$ (PDF#16-0223). It is worth mentioning that the relative intensity of the diffraction peaks of $LiTiO_2$ in Li_2Se-$LiTiO_2$ composite becomes stronger with increasing proportion of $LiTiO_2$ (Figure S1). According to our previous work [34], LiH could react with Se to generate Li_2Se ($2LiH + Se = Li_2Se + H_2 \uparrow$). Analogously, $LiTiO_2$ could be obtained by reacting LiH with TiO_2 ($2LiH + 2TiO_2 = 2LiTiO_2 + H_2 \uparrow$), which is verified by XRD results in Figures 2c and S1. The distinct characteristic peaks of $LiTiO_2$ match well with the cubic phase (Fm3m space group) with lattice parameters of a = b = c = 4.140 Å, which Li and Ti ions are octahedrally coordinated by O [36–38]. The comparison of our work with other recent studies on Li-Se batteries is shown in Table S1. On the on hand, the introduction of TiO_2 alone could improve

the cycling performance, but could not relieve the volume expansion. On the other hand, the traditional pre-lithiation process is excessively complex, and a large number of toxic solvents are used in the preparation process, which seriously pollutes the environment. The synthetic route we adopted is simple, green and environmentally friendly, which has great application prospects.

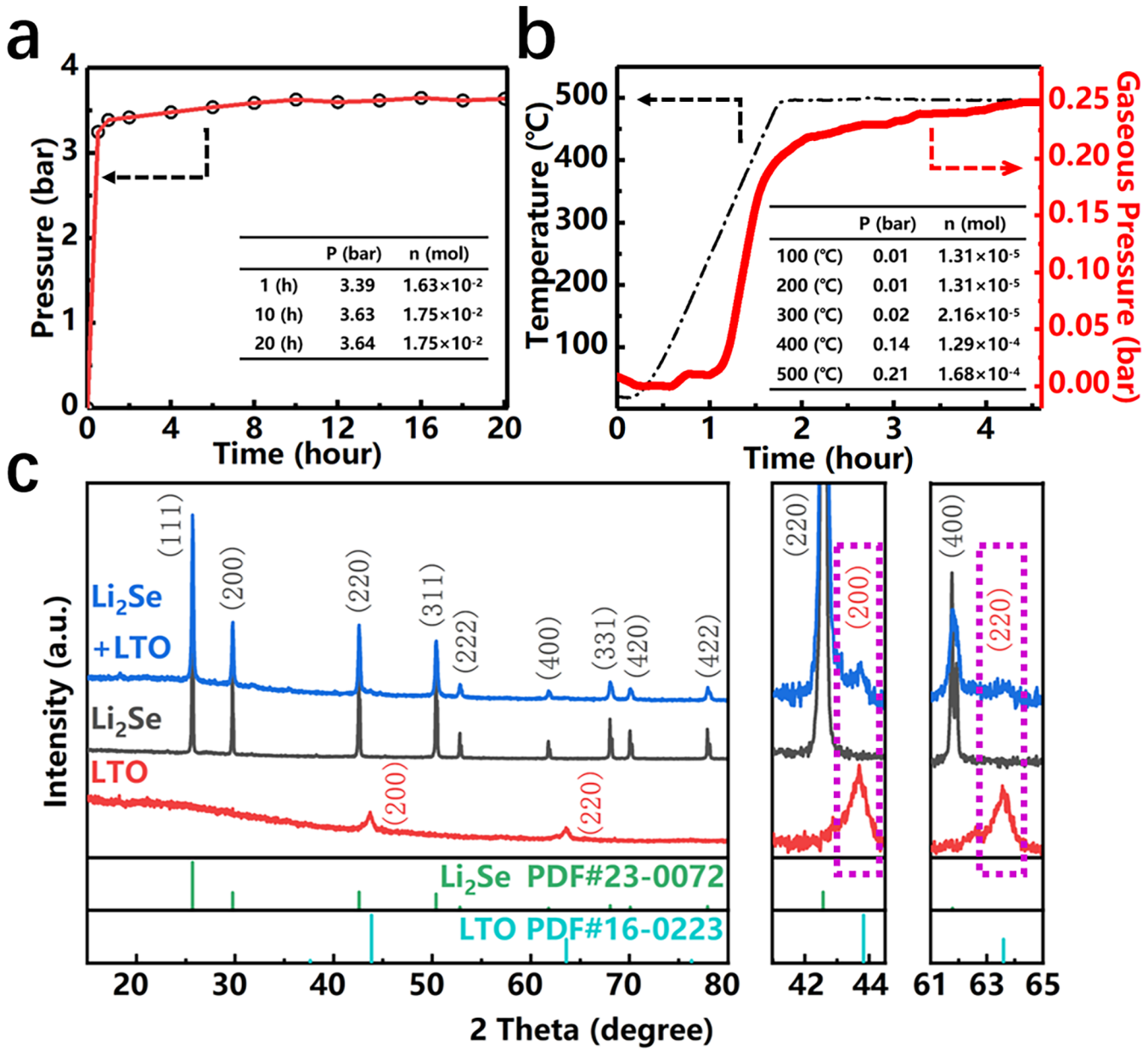

Figure 2. (**a**) Time-pressure curve during ball milling process. The insert table is the pressure and the number of moles in the gas at certain sampling points. (**b**) Time-temperature and time-pressure curves during heating process. The insert table is the pressure and the number of moles in the gas at certain sampling points. (**c**) XRD patterns of Li_2Se-$LiTiO_2$, Li_2Se and $LiTiO_2$.

The microstructure, morphology and elemental distribution of Li_2Se-$LiTiO_2$ are further investigated by SEM, TEM and EDS. Compared to pristine Li_2Se (Figure S2a), Li_2Se-$LiTiO_2$ composite has more regular morphology with small particle size ranging from 60 to 100 nm (Figure 3a,b), which will be favorable to significantly enhance the electrochemical reactivity and structural stability [34]. Additionally, as illustrated in Figure 3d,e, Se signal is uniformly distributed in Li_2Se-$LiTiO_2$ composite, whereas Ti and O signals are tightly conjunct with

each other. This result vividly demonstrates Li_2Se has a good distribution in $LiTiO_2$. Moreover, the surface chemical state of Li_2Se-$LiTiO_2$ composite is elucidated by XPS test. As shown in Figure 3c,f, the peaks of Se-3d and Ti-2p both slightly shift towards the high binding energy since some chemotactic bonds are formed between Li_2Se and $LiTiO_2$, which will weaken the shielding effect of the electron atmosphere. It is worth noting that compared to commercial anatase TiO_2 (Figure S2e), $LiTiO_2$ (Figure 3g) has slightly larger particle size in the range of 60–80 nm with rougher surface and particle agglomeration. This is attributed to the strong collision of TiO_2 particles during the synthesis process. Additionally, the lattice spacings of TiO_2 (Figure S2f,g) are 0.148 nm and 0.149 nm, respectively, corresponding to the (204) and (213) interplanar distances of anatase TiO_2 phase (PDF#21-1272). In contrast, the lattice distances are 0.239 nm and 0.206 nm as shown in Figure 3i, respectively, indexing the (111) and (200) crystal planes of $LiTiO_2$ (PDF#16-0223), thereby further providing the evidence of the existence of $LiTiO_2$ in Li_2Se-$LiTiO_2$ composite.

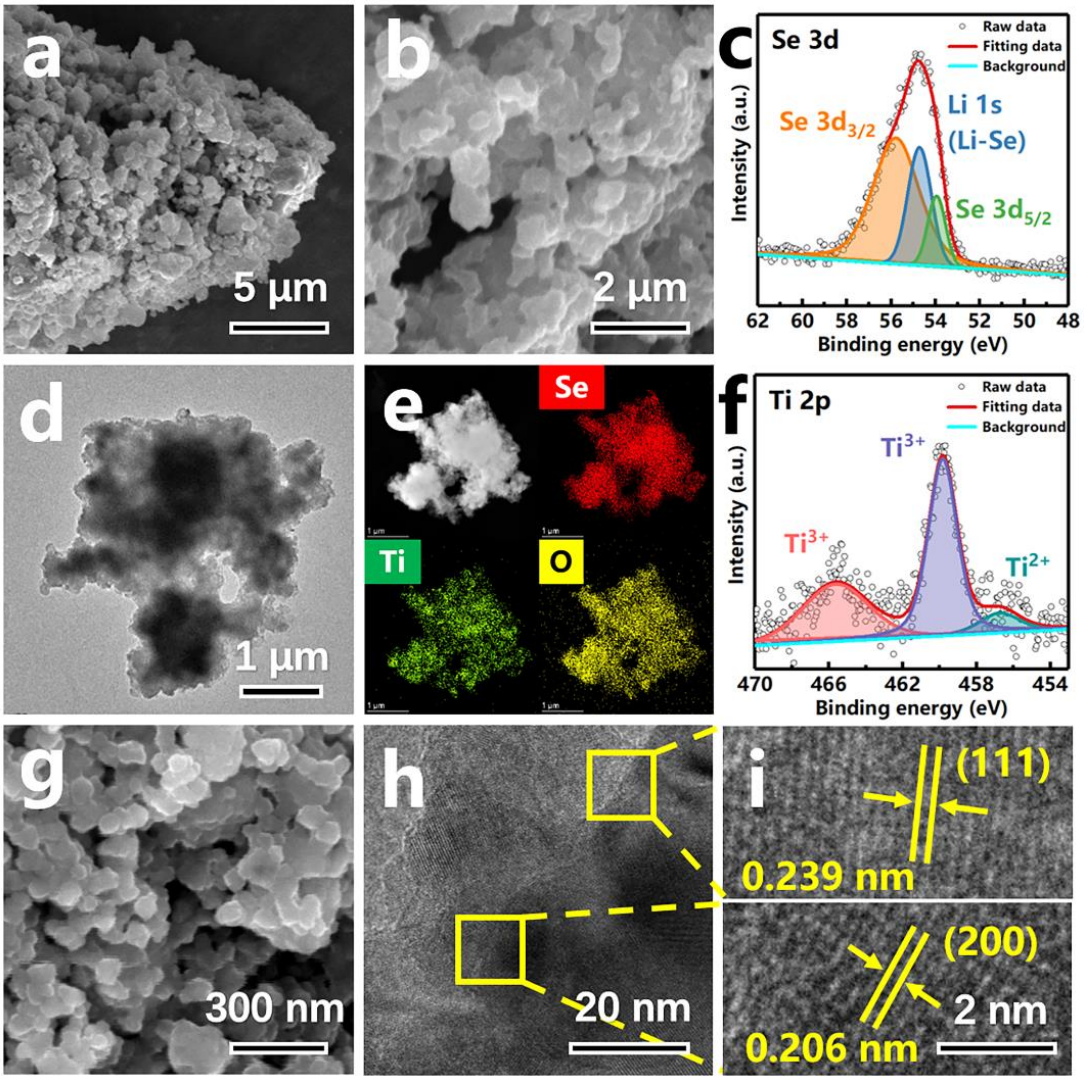

Figure 3. (**a**,**b**) SEM images of Li_2Se-$LiTiO_2$. (**c**,**f**) High-resolution XPS spectra of Se 3d and Ti 2p of Li_2Se-$LiTiO_2$. (**d**) TEM image of Li_2Se-$LiTiO_2$. (**e**) EDS mapping of Li_2Se-$LiTiO_2$. (**g**) SEM image of $LiTiO_2$. (**h**) TEM image of $LiTiO_2$. (**i**) HRTEM images of $LiTiO_2$.

Figure 4a–c presents the CV profiles of Li_2Se-$LiTiO_2$, Li_2Se and $LiTiO_2$ cathodes in the voltage range of 1.7–3.8 V at a scan rate of 0.1 mV s^{-1}. At the first Li^+ extraction step, Li_2Se-$LiTiO_2$ cathode has two adjacent oxidation peaks at 2.27 V and 2.31 V. According to

previous works [17,21,39], the oxidation peaks of $LiTiO_2$ and Li_2Se are generally located at 2.18 V (Figure 4c) and 2.31 V (Figure 4b), which are assigned to the conversion of Ti^{3+} to Ti^{4+} in $LiTiO_2$ and the formation of hexagonal element Se^0 in Li_2Se, respectively. Meanwhile, two-stage processes are observed during the first lithiation step, corresponding to the reduction from Se to polyselenides (2.05 V) and then to Li_2Se/Li_2Se_2 (1.85 V) [19,34]. Noteworthy, the position of reduction peaks after the first cycle slightly moves to the higher potential, implying the overpotential is decreased. This is mainly due to the lower de-lithiated potential of $LiTiO_2$, which triggers the Li^+ extraction of Li_2Se.

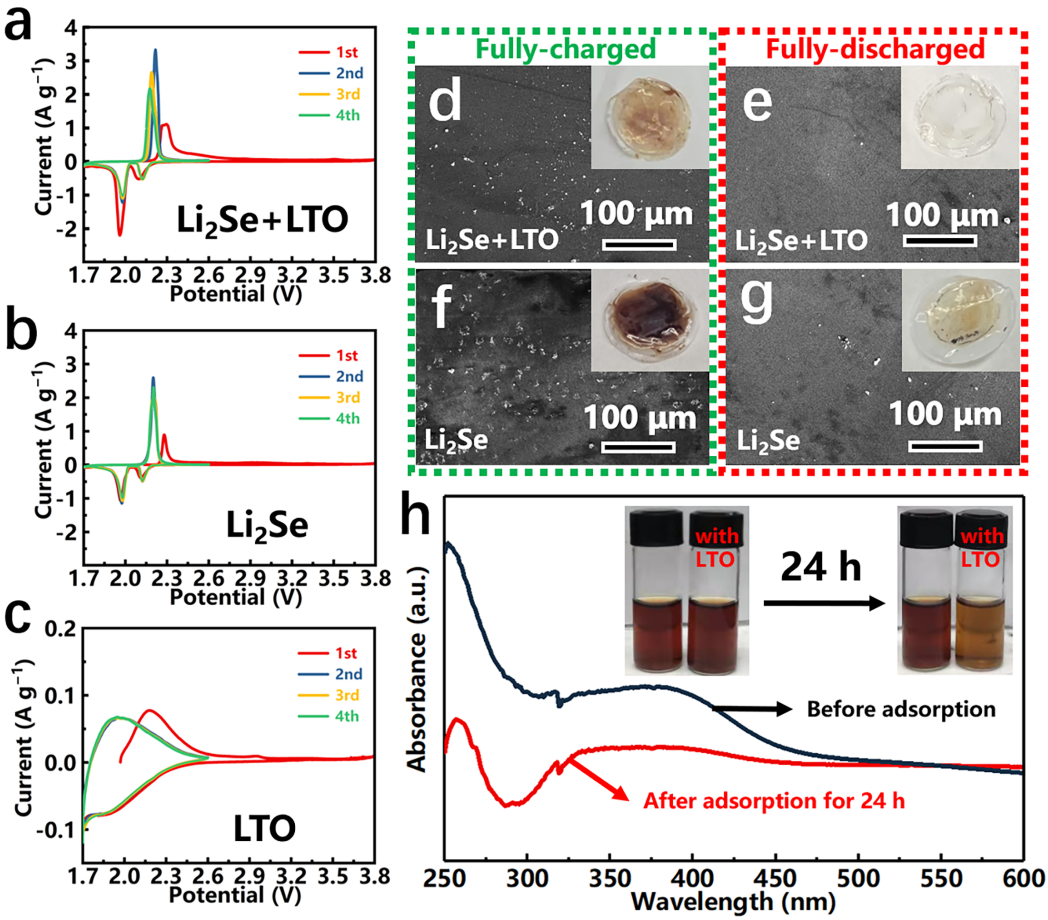

Figure 4. (**a**–**c**) CV profiles of Li_2Se-$LiTiO_2$, Li_2Se and $LiTiO_2$ cathodes. (**d**–**g**) SEM images of Li_2Se-$LiTiO_2$ and Li_2Se cathodes at fully charged/discharged state. The insets are the digital photos of separators. (**h**) UV-vis spectra of Li_2Se_6 solution with $LiTiO_2$ before/after adsorption test.

To further verify the role of $LiTiO_2$ in the Li^+ insert/extract processes of Li_2Se, the color change of separators is examined by digital photos and SEM images. As shown in Figure 4d, in the fully charged state, the separator of Li_2Se-$LiTiO_2$ turns light reddish-brown, as well as only a few of particles are observed at the surface of separator. In contrast, the separator of Li_2Se turns conspicuous brick-red, and many particles appear on the surface of separator as illustrated in Figure 4f. Meanwhile, during the fully discharged state, it shows the similar phenomenon, which the separator of Li_2Se-$LiTiO_2$ sample is much cleaner than that of Li_2Se sample (Figure 4e,g). Apparently, $LiTiO_2$ facilitates the conversion of Li_2Se to Se, and it inhibits the dissolution of polyselenides.

Generally, TiO_2 has good chemisorption on polysulfides/polyselenides for Li-S and Li-Se batteries [14,28–31]. In this work, $LiTiO_2$ is a fully lithiated state of TiO_2, which has very different chemical state to TiO_2. Therefore, it is necessary to inspect the polyselenide adsorption capability of $LiTiO_2$. As depicted in Figure 4h, we design the simulated polyselenide adsorption experiment, which $LiTiO_2$ is added to the simulative Li_2Se_6 solution.

After 24 h, the color of Li_2Se_6 solution changes from dark brown to light brown with adding $LiTiO_2$. Moreover, on the basis of UV-vis result, the characteristic peak intensity is dramatically decreased, reflecting the reduced concentration of Li_2Se_6 in simulated solution. This result clearly indicates that $LiTiO_2$ has superior polyselenides trapping ability, which is favorable to achieve stable electrochemical performance of Li-Se batteries.

The electrochemical performance of Li_2Se-$LiTiO_2$ composite is evaluated by coin cells. Figure 5a–c exhibit the galvanostatic charge-discharge profiles of Li_2Se-$LiTiO_2$, Li_2Se and $LiTiO_2$ cathodes. A noticeable overpotential (2.93 V) can be observed in Li_2Se cathode during the first charge profile, which is related to the obstruction of Li^+ extraction from crystalline Li_2Se and the formation of a new interface [40]. Impressively, the overpotential of Li_2Se-$LiTiO_2$ cathode is dramatically diminished to only 2.15 V. It is probably attributed to the presence of oxygen vacancies, where Ti^{4+} is converted to Ti^{3+} in the synthesis process [41–43]. In the charging process, these oxygen vacancies stabilize the free ions, acting as Lewis acid sites that can interact strongly with polyselenides and release more Li^+ [44,45]. Meanwhile, the overpotential of Li_2Se-TiO_2 cathode is still present (Figure S3a), which further supports our assumptions. In the subsequent charging process, a long plateau at ~2.18 V is observed, which is related to the reversible conversion of Li_2Se_2/Li_2Se to Li_2Se_n ($8 \geq n \geq 4$) and Se [46,47]. Meanwhile, during the discharge process, the Li_2Se, Li_2Se-$LiTiO_2$ and Li_2Se-TiO_2 cathodes have two voltage plateaus located at ~2.12 V and ~2.05 V, respectively, which are ascribed to the multistep phase transitions of Se to soluble long-chain Li_2Se_n ($8 \geq n \geq 4$) and further to insoluble short-chain Li_2Se_2/Li_2Se [48,49]. It is worth noting that when the first charging voltage is 2.6 V, Li_2Se is nonactivated and the Li^+ is not completely detached from Li_2Se, exhibiting terrible cycling performance (Figure S4).

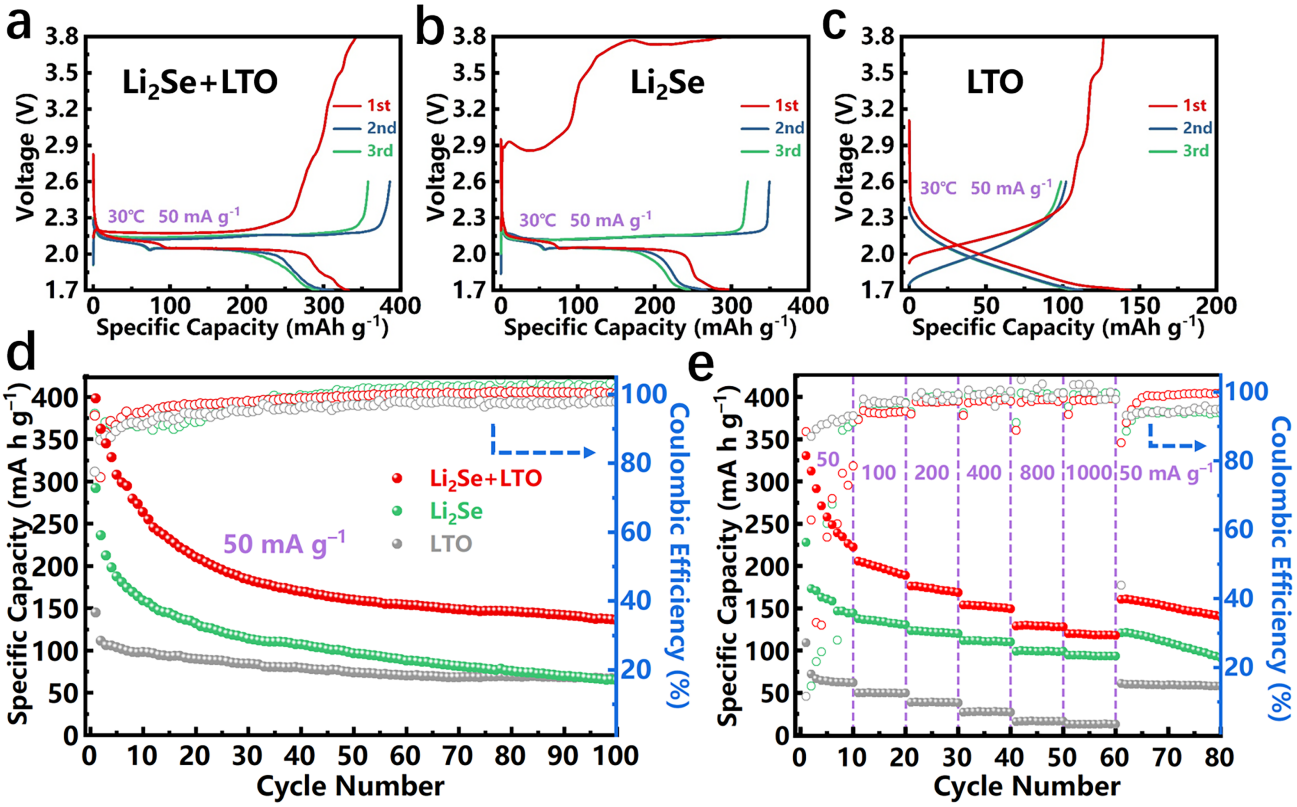

Figure 5. (**a**–**c**) The initial charge-discharge profiles of Li_2Se-$LiTiO_2$, Li_2Se and $LiTiO_2$ electrodes at a current density of 50 mA g^{-1}. (**d**,**e**) Cycling stability at a current density of 50 mA g^{-1} and multi-rate cycling performance of Li_2Se-$LiTiO_2$, Li_2Se and $LiTiO_2$ electrodes.

For the purpose to inspect the long-term cycling stability and multi-rate ability of Li_2Se-$LiTiO_2$ cathode, Li_2Se and $LiTiO_2$ cathodes are employed as counterparts. As shown in Figure 5d, Li_2Se-$LiTiO_2$ cathode delivers a high initial discharge capacity of 398 mA h g^{-1}, which are higher than that of Li_2Se cathode (292 mA h g^{-1}). Noteworthy, the capacity fading of Li_2Se is 19% after 1 cycle, whereas Li_2Se-$LiTiO_2$ cathode is only 9%. The reversible specific capacity of Li_2Se-$LiTiO_2$ cathode still remains at 134 mA h g^{-1} after 100 cycles. In sharp contrast, the specific discharge capacity of Li_2Se cathode rapidly decays to 65 mA h g^{-1} after 100 cycles. Additionally, Li_2Se-$LiTiO_2$ cathode exhibits the better multi-rate capability compared to Li_2Se cathode, which delivers reversible capacities of 330, 206, 176, 154, 129 and 120 mA h g^{-1} with upward current densities of 50, 100, 200, 400, 800 and 1000 mA g^{-1}, respectively. Notably, when the current density is returned to 50 mA g^{-1}, a reversible capacity of 160 mA h g^{-1} is recovered. It should be mentioned that the initial discharge capacity of $LiTiO_2$ is 109 mA h g^{-1}, and it delivers 57 mA h g^{-1} after 100 cycles. However, the $LiTiO_2$ content in composite is 20%, thereby contributing a small capacity in Li_2Se-$LiTiO_2$ cathode. The conductive carbon in the cathode provides few capacities (Figure S5). When the molar ratio of Li_2Se to $LiTiO_2$ is 7 to 3, the discharge capacity of Li_2Se-$LiTiO_2$ cathode drops rapidly to only 152 mA h g^{-1} after the 1st cycle, which is related to the high content of $LiTiO_2$ with low specific capacity. Moreover, the cycling stability and multi-rate performance comparison of Li_2Se-$LiTiO_2$ composites with various $LiTiO_2$ contents are illustrated in Figure S3c. Apparently, the sample with 20% $LiTiO_2$ demonstrates the best cycling stability and rate capability compared to other counterparts.

Nyquist plots further are performed to confirm the reaction kinetics and electrochemical activities of Li_2Se-$LiTiO_2$ cathode before/after cycling. As depicted in Figure S3b, Li_2Se-$LiTiO_2$ and Li_2Se cathodes both have a semicircle in high frequency along with a sloping straight line in low frequency. Generally, the formation of soluble polyselenides during the charging/discharging process causing an irreversible loss of active material and the retention of polyselenides in the electrolyte, thus inhibiting the transfer of charge. After 100 cycles, Li_2Se-$LiTiO_2$ cathode has the smaller semicircle, corresponding to the lower charge transfer resistance than Li_2Se cathode. This is attributed to the introduction of $LiTiO_2$ with strong chemisorption on polyselenides, which significantly reduces the internal resistance and further facilitates the mass transfer process.

To further demonstrate the sustained effect of $LiTiO_2$ in stabilizing cycling performance of Li_2Se, the separators after cycling are examined by digital photos, SEM and EDS mapping (Figure 6a–d). In the fully-charged state, the diffraction peaks of Li_2Se disappear with the conversion of Li_2Se to Se, and the newly appeared peaks may be related to the formation of SEI layer and the production of amorphous Se (Figure S6). A large number of reddish-brown particles are observed on the separator of Li_2Se cathode. However, only a few of particles are detected on the separator of Li_2Se-$LiTiO_2$ cathode. These particles are proved to be polyselenides by EDS mapping characterization. After fully discharging, Se combines with Li^+ to regenerate Li_2Se and diffraction peaks of Li_2Se are observed again (Figure S6). Many particles still remain on the surface of the separator in Li_2Se based cell, whereas the surface of the separator of Li_2Se-$LiTiO_2$ based cell is spotlessly clean that virtually no particles are observed. This result clearly suggests a long-term role of $LiTiO_2$ to suppress the polyselenide migration and strictly confine polyselenides in the cathode side, matching well with the results in Figure 4d–g.

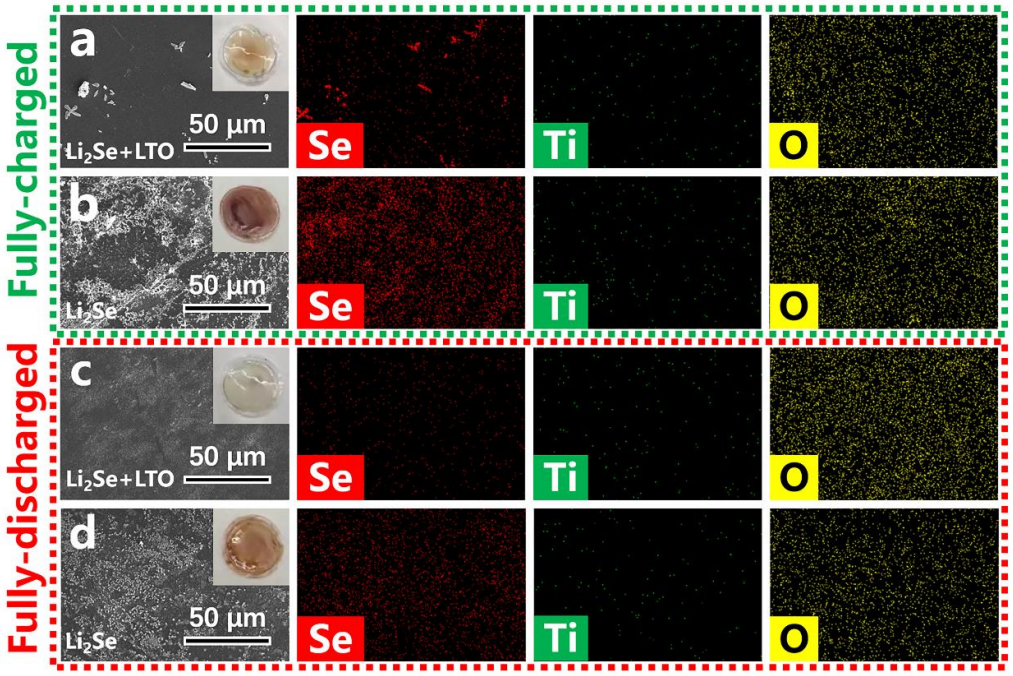

Figure 6. Digital photos, SEM images and EDS mapping of the separators assembled in Li_2Se-$LiTiO_2$ (**a**,**c**) and Li_2Se (**b**,**d**) based cells at fully charged/discharged states after 10 cycles.

4. Conclusions

In summary, an innovative Li_2Se-$LiTiO_2$ composite cathode material is successfully developed by a two-step solid-phase method for advanced Li-Se batteries. $LiTiO_2$ with strong chemical adsorption of polyselenides, emerges oxygen vacancies during the conversion of Ti^{4+} into Ti^{3+}. These oxygen vacancies release of Li^+ from polyselenide and improve the utilization of Se. Li-Se battery with this novel cathode exhibits remarkable electrochemical performance in terms of the reduced overpotential from 2.93 V to 2.15 V and high specific discharge capacity that cathode is two times higher than Li_2Se cathode. This work provides fantastic inspiration for rationally designing fully pre-lithiated Se-based cathodes in advanced Li-Se batteries.

Supplementary Materials: The following supporting information can be downloaded at: https://www.mdpi.com/article/10.3390/nano12050815/s1, Table S1. The comparison of cycling performance for Li-Se batteries based on recent studies. Figure S1. XRD patterns of gradient molar ratio of $LiTiO_2$ in Li_2Se. Figure S2. (a) SEM image of Li_2Se. (b) SEM image of $LiTiO_2$. (c) High-resolution XPS spectrum of Se 3d region in Li_2Se. (d) High-resolution XPS spectrum of Ti 2p region in $LiTiO_2$. (e) SEM image of TiO_2. (f) TEM image of TiO_2. (g) HR-TEM images of TiO_2. Figure S3. (a) The initial charge-discharge profiles of Li_2Se-TiO_2 at a current density of 50 mA g^{-1}. (b) Nyquist plots before/after cycling of Li_2Se-$LiTiO_2$ and Li_2Se. (c–d) Cycling stability at a current density of 50 mA g^{-1} and multi-rate cycling performance of gradient molar ratio of $LiTiO_2$ in Li_2Se electrodes. Figure S4. (a) The charge-discharge profiles of Li_2Se-$LiTiO_2$ at 1.7–2.6 V. (b) Cycling stability of Li_2Se-$LiTiO_2$ at 1.7–2.6 V with a current density of 50 mA g^{-1}. Figure S5. The initial charge-discharge profiles of conductive carbon at a current density of 50 mA g^{-1}. Figure S6. XRD patterns of Li_2Se-$LiTiO_2$ cathodes after charged/discharged.

Author Contributions: Conceptualization, Y.X.; Funding Acquisition, Y.X. and W.Z.; Writing-Original Draft, Y.X. and Z.F.; Methodology, Z.F. and X.H.; Investigation, Z.F., Z.X. and G.W.; Formal analysis, C.L., Z.X., X.H., Y.G., H.H. and G.W.; Data Curation, C.L. and X.H.; Writing-Review and Editing, C.L. and W.Z.; Visualization, Y.G., H.H. and G.W., Supervision, W.Z. All authors have read and agreed to the published version of the manuscript.

Funding: This research was funded by Zhejiang Provincial Natural Science Foundation of China (LY21E020005, 2022C01173 and LD22E020006), China Postdoctoral Science Foundation (2020M671785

and 2020T130597), National Natural Science Foundation of China (U20A20253, 21972127 and 21905249) and Zhejiang Provincial Special Support Program for High-level Talents (2020R51004).

Data Availability Statement: Data can be available upon request from the authors.

Conflicts of Interest: The authors declare are no conflict of interest.

References

1. Ghosh, A.; Cherepanov, P.; Nguyen, C.; Ghosh, A.; Kumar, A.; Ahuja, A.; Kar, M.; MacFarlane, D.R.; Mitra, S. Simple route to lithium dendrite prevention for long cycle-life lithium metal batteries. *Appl. Mater. Today* **2021**, *23*, 101062. [CrossRef]
2. Liu, K.; Wang, Z.; Shi, L.; Jungsuttiwong, S.; Yuan, S. Ionic liquids for high performance lithium metal batteries. *J. Energy Chem.* **2021**, *59*, 320–333. [CrossRef]
3. Dong, H.; Wang, Y.; Tang, P.; Wang, H.; Li, K.; Yin, Y.; Yang, S. A novel strategy for improving performance of lithium-oxygen batteries. *J. Colloid Interface Sci.* **2021**, *584*, 246–252. [CrossRef] [PubMed]
4. Chen, Y.; Wang, T.; Tian, H.; Su, D.; Zhang, Q.; Wang, G. Advances in Lithium–Sulfur Batteries: From Academic Research to Commercial Viability. *Adv. Mater.* **2021**, *33*, e2003666. [CrossRef] [PubMed]
5. Yang, Z.; Jia, D.; Wu, Y.; Song, D.; Sun, X.; Wang, C.; Yang, L.; Zhang, Y.; Gao, J.; Ohsaka, T.; et al. Novel lithium-chalcogenide batteries combining S, Se and C characteristics supported by chitosan-derived carbon intertwined with CNTs. *Chem. Eng. J.* **2022**, *427*, 131790. [CrossRef]
6. Atin, P.; Sandipan, M.; Sourindra, M. Metal hydroxides as a conversion electrode for lithium-ion batteries: A case study with a $Cu(OH)_2$ nanoflower array. *J. Mater. Chem. A* **2014**, *2*, 18515–18522. [CrossRef]
7. Lu, J.; Chen, Z.; Pan, F.; Cui, Y.; Amine, K. High-Performance Anode Materials for Rechargeable Lithium-Ion Batteries. *Electrochem. Energy Rev.* **2018**, *1*, 35–53. [CrossRef]
8. Naoki, N.; Wu, F.; Jung, T.L.; Gleb, Y. Li-ion battery materials: Present and future. *Mater. Today* **2015**, *18*, 252–264. [CrossRef]
9. Atin, P.; Shreyasi, C.; Goutam, D.; Sourindra, M. Efficient energy storage in mustard husk derived porous spherical carbon nanostructures. *Mater. Adv.* **2021**, *2*, 7463–7472. [CrossRef]
10. Liu, Y.; Chatterjee, A.; Rusch, P.; Wu, C.; Nan, P.; Peng, M.; Bettels, F.; Li, T.; Ma, C.; Zhang, C.; et al. Monodisperse Molybdenum Nanoparticles as Highly Efficient Electrocatalysts for Li-S Batteries. *ACS Nano* **2021**, *15*, 15047–15056. [CrossRef]
11. Tang, T.; Hou, Y. Chemical Confinement and Utility of Lithium Polysulfides in Lithium Sulfur Batteries. *Small Methods* **2019**, *4*, 1900001. [CrossRef]
12. Baek, M.; Shin, H.; Char, K.; Choi, J.W. New High Donor Electrolyte for Lithium–Sulfur Batteries. *Adv. Mater.* **2020**, *32*, e2005022. [CrossRef] [PubMed]
13. Li, M.; Lu, J.; Amine, K. Nanotechnology for Sulfur Cathodes. *ACS Nano* **2021**, *15*, 8087–8094. [CrossRef]
14. Zhao, K.; Jin, Q.; Zhang, L.; Li, L.; Wu, L.; Zhang, X. Achieving dendrite-free lithium deposition on the anode of Lithium–Sulfur battery by LiF-rich regulation layer. *Electrochim. Acta* **2021**, *393*, 138981. [CrossRef]
15. Lin, S.; Chen, Y.; Wang, Y.; Cai, Z.; Xiao, J.; Muhmood, T.; Hu, X. Three-Dimensional Ordered Porous Nanostructures for Lithium–Selenium Battery Cathodes That Confer Superior Energy-Storage Performance. *ACS Appl. Mater. Interfaces* **2021**, *13*, 9955–9964. [CrossRef]
16. Wang, Y.; Huang, X.; Zhang, S.; Hou, Y. Sulfur Hosts against the Shuttle Effect. *Small Methods* **2018**, *2*, 1700345. [CrossRef]
17. Zhao, X.; Jiang, L.; Ma, C.; Cheng, L.; Wang, C.; Chen, G.; Yue, H.; Zhang, D. The synergistic effects of nanoporous fiber TiO_2 and nickel foam interlayer for ultra-stable performance in lithium-selenium batteries. *J. Power Sources* **2021**, *490*, 229534. [CrossRef]
18. Xiang, H.; Deng, N.; Zhao, H.; Wang, X.; Wei, L.; Wang, M.; Cheng, B.; Kang, W. A review on electronically conducting polymers for lithium-sulfur battery and lithium-selenium battery: Progress and prospects. *J. Energy Chem.* **2021**, *58*, 523–556. [CrossRef]
19. Cao, Y.; Lei, F.; Li, Y.; Qiu, S.; Wang, Y.; Zhang, W.; Zhang, Z. A MOF-derived carbon host associated with Fe and Co single atoms for Li–Se batteries. *J. Mater. Chem. A* **2021**, *9*, 16196–16207. [CrossRef]
20. Deng, N.; Feng, Y.; Wang, G.; Wang, X.; Wang, L.; Li, Q.; Zhang, L.; Kang, W.; Cheng, B.; Liu, Y. Rational structure designs of 2D materials and their applications toward advanced lithium-sulfur battery and lithium-selenium battery. *Chem. Eng. J.* **2020**, *401*, 125976. [CrossRef]
21. Jin, J.; Tian, X.; Srikanth, N.; Kong, L.B.; Zhou, K. Advances and challenges of nanostructured electrodes for Li–Se batteries. *J. Mater. Chem. A* **2017**, *5*, 10110–10126. [CrossRef]
22. Huang, X.L.; Guo, Z.; Dou, S.X.; Wang, Z.M. Rechargeable Potassium–Selenium Batteries. *Adv. Funct. Mater.* **2021**, *31*, 2102326. [CrossRef]
23. Tang, S.; Liu, C.; Sun, W.; Zhang, X.; Shen, D.; Dong, W.; Yang, S. Understanding the anchoring and catalytic effect of the $Co@C_2N$ monolayer in lithium–selenium batteries: A first-principles study. *Nanoscale* **2021**, *13*, 16316–16323. [CrossRef]
24. Fang, Y.; Luan, D.; Gao, S.; Lou, X.W. Rational Design and Engineering of One-Dimensional Hollow Nanostructures for Efficient Electrochemical Energy Storage. *Angew. Chem. Int. Ed.* **2021**, *60*, 20102–20118. [CrossRef] [PubMed]
25. Huang, X.L.; Zhou, C.; He, W.; Sun, S.; Chueh, Y.-L.; Wang, Z.M.; Liu, H.K.; Dou, S.X. An Emerging Energy Storage System: Advanced Na–Se Batteries. *ACS Nano* **2021**, *15*, 5876–5903. [CrossRef]

26. Li, C.; Wang, Y.; Li, H.; Liu, J.; Song, J.; Fusaro, L.; Hu, Z.-Y.; Chen, Y.; Li, Y.; Su, B.-L. Weaving 3D highly conductive hierarchically interconnected nanoporous web by threading MOF crystals onto multi walled carbon nanotubes for high performance Li–Se battery. *J. Energy Chem.* **2021**, *59*, 396–404. [CrossRef]
27. Wu, K.; Wang, J.; Xu, C.; Jiao, X.; Hu, X.; Guan, W. Hollow Spherical α-MoO_3: An Effective Electrocatalyst of Polyselenides for Lithium–Selenium Batteries. *ACS Appl. Energy Mater.* **2021**, *4*, 10203–10212. [CrossRef]
28. Zhang, Z.; Zhang, Z.; Zhang, K.; Yang, X.; Li, Q. Improvement of electrochemical performance of rechargeable lithium–selenium batteries by inserting a free-standing carbon interlayer. *RSC Adv.* **2014**, *4*, 15489–15492. [CrossRef]
29. Liu, N.; Ma, H.; Wang, L.; Zhao, Y.; Bakenov, Z.; Wang, X. Dealloying-derived nanoporous deficient titanium oxide as high-performance bifunctional sulfur host-catalysis material in lithium-sulfur battery. *J. Mater. Sci. Technol.* **2021**, *84*, 124–132. [CrossRef]
30. Gui, Y.; Chen, P.; Liu, D.; Fan, Y.; Zhou, J.; Zhao, J.; Liu, H.; Guo, X.; Liu, W.; Cheng, Y. TiO_2 nanotube/RGO modified separator as an effective polysulfide-barrier for high electrochemical performance Li-S batteries. *J. Alloys Compd.* **2021**, *895*, 162495. [CrossRef]
31. Xia, Y.; Ren, Q.; Lu, C.; Zhu, J.; Zhang, J.; Liang, C.; Huang, H.; Gan, Y.; He, X.; Zhu, D.; et al. Graphene/TiO_2 decorated N-doped carbon foam as 3D porous current collector for high loading sulfur cathode. *Mater. Res. Bull.* **2021**, *135*, 111129. [CrossRef]
32. Lei, Z.; Lei, Y.; Liang, X.; Yang, L.; Feng, J. High stable rate cycling performances of microporous carbon spheres/selenium composite (MPCS/Se) cathode as lithium–selenium battery. *J. Power Sources* **2020**, *473*, 228611. [CrossRef]
33. Wu, F.; Lee, J.T.; Xiao, Y.; Yushin, G. Nanostructured Li_2Se cathodes for high performance lithium-selenium batteries. *Nano Energy* **2016**, *27*, 238–246. [CrossRef]
34. Lu, C.; Zhang, W.; Fang, R.; Xiao, Z.; Huang, H.; Gan, Y.; Zhang, J.; He, X.; Liang, C.; Zhu, D.; et al. Facile and efficient synthesis of Li_2Se particles towards high-areal capacity Li2Se cathode for advanced Li–Se battery. *Sustain. Mater. Technol.* **2021**, *29*, e00288. [CrossRef]
35. Bui, H.T.; Jang, H.; Ahn, D.; Han, J.; Sung, M.; Kutwade, V.; Patil, M.; Sharma, R.; Han, S.-H. High-performance Li–Se battery: Li_2Se cathode as intercalation product of electrochemical in situ reduction of multilayer graphene-embedded 2D-$MoSe_2$. *Electrochim. Acta* **2020**, *368*, 137556. [CrossRef]
36. Koudriachova, M. Ramsdellite-structured $LiTiO_2$: A new phase predicted from ab initio calculations. *Chem. Phys. Lett.* **2008**, *458*, 108–112. [CrossRef]
37. Yang, H.-D.; Kang, Y.-Y.; Zhu, P.-P.; Chen, Q.-W.; Yang, L.; Zhou, J.-P. Facile hydrothermal preparation, characterization and multifunction of rock salt-type $LiTiO_2$. *J. Alloys Compd.* **2021**, *872*, 159759. [CrossRef]
38. Mackrodt, W. First Principles Hartree–Fock Description of Lithium Insertion in Oxides: I. The End Members TiO_2 and $LiTiO_2$ of the System $LixTiO_2$. *J. Solid State Chem.* **1999**, *142*, 428–439. [CrossRef]
39. Wang, D.; Zhang, G.; Shan, Z.; Zhang, T.; Tian, J. Hierarchically Micro-/Nanostructured TiO_2/Micron Carbon Fibers Composites for Long-Life and Fast-Charging Lithium-Ion Batteries. *ChemElectroChem* **2018**, *5*, 540–545. [CrossRef]
40. Zhou, L.; Zhang, W.; Wang, Y.; Liang, S.; Gan, Y.; Huang, H.; Zhang, J.; Xia, Y.; Liang, C. Lithium Sulfide as Cathode Materials for Lithium-Ion Batteries: Advances and Challenges. *J. Chem.* **2020**, *2020*, 1–17. [CrossRef]
41. Chen, X.; Liu, L.; Yu, P.Y.; Mao, S.S. Increasing Solar Absorption for Photocatalysis with Black Hydrogenated Titanium Dioxide Nanocrystals. *Science* **2011**, *331*, 746–750. [CrossRef] [PubMed]
42. Chen, X.; Liu, L.; Huang, F. Black titanium dioxide (TiO_2) nanomaterials. *Chem. Soc. Rev.* **2015**, *44*, 2019. [CrossRef] [PubMed]
43. Kim, D.; Hong, J.; Park, Y.R.; Kim, K.J. The origin of oxygen vacancy induced ferromagnetism in undoped TiO_2. *J. Phys. Condens. Matter* **2009**, *21*, 195405. [CrossRef] [PubMed]
44. Li, C.; Huang, Y.; Chen, C.; Feng, X.; Zhang, Z. High-performance polymer electrolyte membrane modified with isocyanate-grafted Ti^{3+} doped TiO_2 nanowires for lithium batteries. *Appl. Surf. Sci.* **2021**, *563*, 150248. [CrossRef]
45. Zhu, W.-D.; Wang, C.-W.; Chen, J.-B.; Li, Y.; Wang, J. Enhanced field emission from Ti^{3+} self-doped TiO_2 nanotube arrays synthesized by a facile cathodic reduction process. *Appl. Surf. Sci.* **2014**, *301*, 525–529. [CrossRef]
46. Singh, A.; Kalra, V. Electrospun nanostructures for conversion type cathode (S, Se) based lithium and sodium batteries. *J. Mater. Chem. A* **2019**, *7*, 11613–11650. [CrossRef]
47. Jin, W.-W.; Li, H.-J.; Zou, J.-Z.; Inguva, S.; Zhang, Q.; Zeng, S.-Z.; Xu, G.-Z.; Zeng, X.-R. Metal organic framework-derived carbon nanosheets with fish-scale surface morphology as cathode materials for lithium–selenium batteries. *J. Alloys Compd.* **2020**, *820*, 153084. [CrossRef]
48. Ma, C.; Wang, H.; Zhao, X.; Wang, X.; Miao, Y.; Cheng, L.; Wang, C.; Wang, L.; Yue, H.; Zhang, D. Porous Bamboo-Derived Carbon as Selenium Host for Advanced Lithium/Sodium–Selenium Batteries. *Energy Technol.-Ger.* **2020**, *8*, 1901445. [CrossRef]
49. Wang, Y.; Ke, C.; Zhou, J.; Qin, L.; Lin, X.; Cheng, Q.; Liu, J. N-doped C/Se derived from a Cu-based coordination polymer as cathode for lithium-selenium batteries. *Inorg. Chem. Commun.* **2019**, *108*, 107537. [CrossRef]